

Transient Growth in an Airfoil Separation Bubble

S. A. Loh¹, H. M. Blackburn¹ and S. J. Sherwin²

¹Department of Mechanical and Aerospace Engineering
Monash University, Victoria 3800, Australia

²Department of Aeronautics
Imperial College, London SW7 2AZ, United Kingdom

Abstract

In this work, transient growth in a laminar separation bubble in a low-to-moderate Reynolds number airfoil flow is investigated. Optimal two and three-dimensional initial perturbations are computed for the flow over a NACA 0012 airfoil at angle-of-attack $\alpha = 5^\circ$ with chord based $Re = 5 \times 10^4$. At this Reynolds number, the pressure surface boundary layer remains attached over the length of the airfoil while the suction surface boundary layer undergoes separation before becoming two-dimensionally unstable leading to periodic vortex shedding and reattachment. Transient growth analysis shows that this flow supports large energy growth for both two and three-dimensional perturbations. Optimal growth values and flow topologies show that two-dimensional mechanisms are the primary energy growth mechanisms. Upstream of vortex shedding, the primary growth mechanism appears to be the Orr mechanism while a separate mechanism appears to drive further energy growth downstream in the base flow shed vorticity.

Introduction

Low to moderate Reynolds number airfoil flows have become increasingly important due to recent interest and advances in unmanned and micro air vehicle design. In these flows, laminar separation bubbles (LSBs) are commonly formed through a process of boundary layer separation, transition to turbulence and reattachment. The performance of an airfoil in such a flow can critically depend on the characteristics of an LSB and hence the mechanics of the transition process.

Recent numerical studies have begun to explore this process in airfoil type geometries. At very low Reynolds number, Theofilis *et al.*[9] conducted a BiGlobal stability analysis of the steady LSB in flow over a NACA 0012 airfoil and identified a wake instability as the leading instability mode. Kitsios *et al.*[6] and Abdessemed *et al.*[1] identified this mode, as well as a three-dimensional stationary mode in flows over a NACA 0015 airfoil and through a periodic array of low-pressure turbine blades respectively. Secondary instability of the unsteady LSBs formed by the onset of vortex shedding due to primary wake instability was also considered in [1]. Weak secondary instability was identified almost immediately after the onset of primary instability at $Re = 905$. The growth rate of the secondary instability was not found to grow significantly with Re , and was shown to be associated with the periodic boundary condition raising questions about its physical relevance.

Steady LSBs near the onset of primary instability were also found to support transient growth of order 10^5 in [1]. Sharma *et al.*[8] examined transient growth in the unsteady flow regime for the same configuration and found similar results. Two-dimensional perturbations were found to be dominant over long time horizons while three-dimensional perturbations of short spanwise wavelength were dominant over short time intervals.

At a higher Reynolds number Jones *et al.*[4] used DNS and clas-

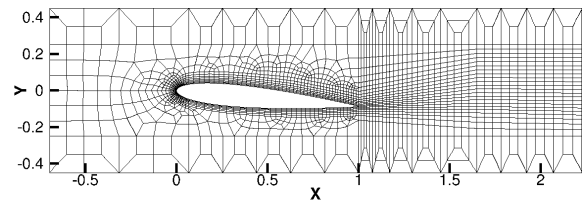


Figure 1. Spectral element mesh used for base flow and stability computations.

sical linear stability to analyze the LSB in flow over a NACA 0012 airfoil at 5 degrees angle-of-attack and $Re = 5 \times 10^4$. Though no absolute instability was detected, a global instability mechanism was identified in DNS simulations using volume forcing to directly perturb the boundary layer. The instability mechanism involved upstream advection of perturbations in the braid region between shed vortices, relying on strong reverse flow and perturbation growth to self-sustain. In a separate work, Jones *et al.*[5] also investigated acoustic receptivity in the same flow and identified an acoustic feedback loop involving the trailing edge as a source and the leading edge as a receptivity site. They suggest that this global instability mechanism may play a role in determining the frequency of vortex shedding associated with the LSB.

To examine the effect of vortical perturbations, Zaki *et al.*[10] reported on DNS simulations of flow over a compressor blade with and without the presence of free-stream turbulence. By varying the intensity of free-stream turbulence introduced at the inflow, different transition mechanisms were observed in the LSB on the suction surface of the blade while the LSB on the pressure side was completely eliminated by transition in the attached boundary layer.

It is clear from the above studies that transition in LSBs in airfoil flows is a complex process, is sensitive to various factors and can occur in a variety of ways. In this work, the role of transient growth mechanisms in an airfoil LSB are investigated at $Re = 5 \times 10^4$. In contrast to previous studies we apply a global stability approach at a Reynolds number sufficient to separate LSB dynamics from wake dynamics.

Formulation

The objective of transient growth analysis is to compute linear perturbations maximizing energy growth over a finite time interval τ . The formulation of the optimal initial perturbation for transient growth is well established but a brief description is provided here. The interested reader is directed to [2] for more detailed discussions.

In this work, we consider the evolution of infinitesimal perturbations $\mathbf{u} = (u(x, y, z, t), v(x, y, z, t), w(x, y, z, t))^T$ to a two-dimensional base flow $\mathbf{U} = (U(x, y, t), V(x, y, t), 0)^T$. The base flow is a time-periodic solution of the incompressible Navier-

Stokes equations computed *a priori* while the perturbation is governed by the linearized Navier–Stokes (LNS) equations:

$$\partial_t \mathbf{u} = -\mathbf{U} \cdot \nabla \mathbf{u} - (\nabla \mathbf{U})^T \cdot \mathbf{u} - \nabla p + Re^{-1} \nabla^2 \mathbf{u}, \quad (1a)$$

$$\nabla \cdot \mathbf{u} = 0. \quad (1b)$$

The perturbation energy growth to maximize over a finite time interval is written:

$$G(\tau) = \frac{(\mathbf{u}(\tau), \mathbf{u}(\tau))}{(\mathbf{u}(0), \mathbf{u}(0))}, \quad (2)$$

where the inner product is the volume integral over the flow domain Ω given by:

$$(\mathbf{u}, \mathbf{u}) = \int_{\Omega} \mathbf{u} \cdot \mathbf{u} dV. \quad (3)$$

Through (1b), the pressure term in (1a) can be eliminated so the LNS equations can be expressed compactly as:

$$\partial_t \mathbf{u} - L(\mathbf{u}) = 0, \quad (4)$$

where L is a linear operator. We then introduce the state transition operator, $\mathcal{A}(\tau) = \exp(Lt)$, to evolve an arbitrary initial perturbation $\mathbf{u}(0)$ to time τ :

$$\mathbf{u}(\tau) = \mathcal{A}(\tau)\mathbf{u}(0). \quad (5)$$

It can be shown that substitution of (5) into (2) leads to:

$$G(\tau) = \frac{(\mathbf{u}(0), \mathcal{A}^*(\tau)\mathcal{A}(\tau)\mathbf{u}(0))}{(\mathbf{u}(0), \mathbf{u}(0))}, \quad (6)$$

where $\mathcal{A}^*(\tau)$ is the adjoint evolution operator of \mathcal{A} whose action evolves an adjoint variable, \mathbf{u}_*^* , from time τ to 0 (see [2]). The optimal growth problem can then be formally stated as:

$$G(\tau) = \max_{\mathbf{u}(0)} \frac{(\mathbf{u}(0), \mathcal{A}^*(\tau)\mathcal{A}(\tau)\mathbf{u}(0))}{(\mathbf{u}(0), \mathbf{u}(0))}, \quad (7)$$

where $G(\tau)$ is given by the largest eigenvalue of the operator $\mathcal{A}^*\mathcal{A}$ while the optimal initial perturbation is given by the corresponding eigenvector.

Methodology

The airfoil considered here is a NACA 0012 at an angle-of-attack $\alpha = 5^\circ$ with chord based $Re = 5 \times 10^4$. Length scales are non-dimensionalized by the airfoil chord, c , while velocities are normalized by the free-stream velocity, \mathbf{U}_∞ . To compute the two-dimensional base flow, DNS of the incompressible Navier–Stokes equations were carried out with a spectral element-Fourier method detailed elsewhere [3]. For the base flow, the streamwise and cross-stream directions, x and y , are discretized using spectral elements while the Fourier decomposition in span, z , is not used due to the two-dimensional nature of the flow. The flow domain is $5.5c \times 5.6c$ in the x and y directions respectively and a close-up of the mesh near the airfoil is shown in figure 1.

To solve the optimal growth problem, a Krylov/Arnoldi method is used to iteratively find dominant eigenvalues/eigenvectors of

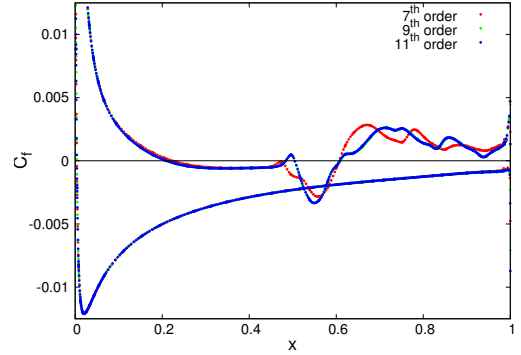


Figure 2. Variation of mean friction coefficient profile with interpolating polynomial order. Top curve is C_f for suction side of airfoil, bottom curve is $-C_f$ for pressure side.

$\mathcal{A}^*\mathcal{A}$ by repeated application of the operator to a random initial perturbation. Rather than directly computing the action of $\mathcal{A}^*\mathcal{A}$ on an initial perturbation by matrix–vector multiplication, the action of $\mathcal{A}^*\mathcal{A}$ is computed by timestepping the LNS equations and their adjoint. This is achieved by evolving an initial perturbation, $\mathbf{u}(0)$, to time τ via the LNS equations, and then evolving the terminal condition, $\mathbf{u}(\tau)$, to time 0 via the adjoint LNS equations. The numerics used for these computations are the same as those used for the base flow, with modifications to solve the LNS or adjoint LNS equations instead of the incompressible Navier–Stokes equations.

The Fourier decomposition in span means the three-dimensional perturbations are of the form:

$$\mathbf{u}(x, y, z, t) = \mathbf{u}(x, y, t) \exp(i\beta z), \quad (8)$$

where superposition allows each Fourier mode to be analysed separately. In this work the response of the base flow is analysed for two-dimensional perturbations with infinite spanwise wavelength, as well as three-dimensional perturbations with spanwise wavelengths from $0.05c$ to $10.0c$. The time intervals chosen for the analysis are $\tau = 0.25T$, $0.5T$ and $1.0T$ where T is the base flow period. These intervals are chosen to avoid perturbation dynamics associated with the wake.

Results

Convergence of the base flow has been determined by comparing mean C_f profiles computed with different interpolating polynomial orders as shown in figure 2. While a polynomial order of 9 appears sufficient for convergence, the results presented here are computed with 11th order polynomials for maximum accuracy. The mean C_f profiles shown in figure 2 also show the separation and reattachment behaviour of the base flow. On the pressure surface of the airfoil, boundary layer attachment is maintained for the length of the airfoil while on the suction surface, a primary separation bubble is seen from $x = 0.21c$ to $x = 0.61c$ and a short secondary separation bubble is observed from $x = 0.48c$ to $x = 0.51c$.

Examination of instantaneous flow data shows the complicated dynamics of this flow. The flow is periodic with a temporal frequency of 1.27. Snapshots of the base flow vorticity field shown in figure 3 suggest that the separated shear layer becomes unstable to a Kelvin–Helmholtz type instability leading to shear layer roll-up and vortex shedding. The shed vortices are then observed to periodically merge as seen in figures 3c and 3d.

Results of the two-dimensional transient growth analysis show

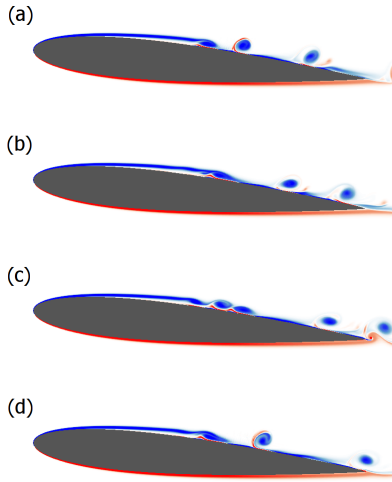


Figure 3. Snapshots of base flow vorticity at points in the base flow limit cycle. Phase points are (a) $t = 0T$; (b) $t = 0.25T$; (c) $t = 0.5T$ and (d) $t = 0.75T$ where T is the base flow period. 100 equispaced contour levels are used between $\omega_z = \pm 100$.

significant amplification of two-dimensional perturbations for all time horizons. Figure 4 shows the variation of optimal growth with time interval for the three cases considered. For the time intervals considered, the flow shows a monotonic increase in energy growth with increases in time interval. For the largest time interval, the growth is around six orders of magnitude larger than the growth observed for the smallest interval.

Vorticity contours for a typical optimal initial condition are shown in 5a. The optimal initial condition is characterized by fine scale upstream tilted vortices in the boundary layer upstream of the primary separation point. This suggests that the Orr mechanism is a primary mechanism of energy growth. The evolution of the optimal initial condition is shown in figures 5a to 5d where tilting and amplification of these structures by the mean shear is evident. At the final time, the perturbation flow structures appear fully entrained in the base flow shed vorticity. Comparison of figures 5c and 5d suggests that some perturbation structures are either damped in the vortex shedding region or merge as they interact with the shed vortex. The implication here is that in addition to the Orr mechanism, another mechanism in the shed vorticity may be driving large transient growth.

When comparing the perturbation snapshots with the base flow snapshots, it is evident that the perturbations end up in the shed vortex resulting from vortex merging, while no perturbation amplitude is visible in the unmerged vortices upstream and downstream of this. This suggests that optimal growth in this flow may be sensitive to variation in base flow phase.

For the short time horizon case, the optimal initial condition shown in figure 6 is structurally similar except for a downstream shift of the tilted spanwise vortices and the addition of significant initial perturbation amplitude in the base flow shed vorticity. This suggests that two areas of perturbation growth are present since over a short time horizon a perturbation amplified upstream may not reach the downstream region to be further amplified. As a result a more equal weighting of initial perturbation amplitude would be expected.

Results of the three-dimensional transient growth analysis show that the flow is still able to support strong transient growth, but two-dimensional perturbations excite larger flow response for all time horizons considered. Figure 7 shows a representative result for the variation of optimal energy growth with perturbation spanwise wavelength. For this case, long wavelength per-

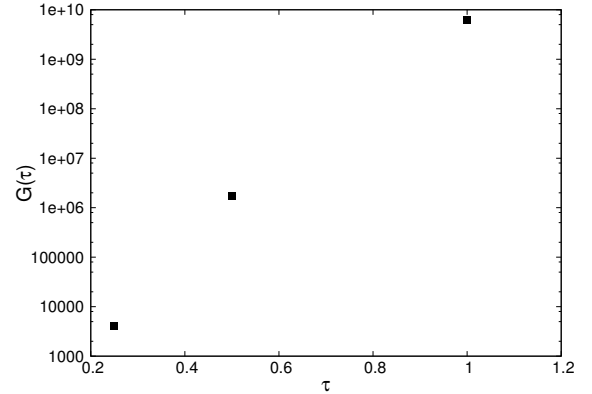


Figure 4. Optimal growth of two-dimensional perturbations for the three time horizons considered here.

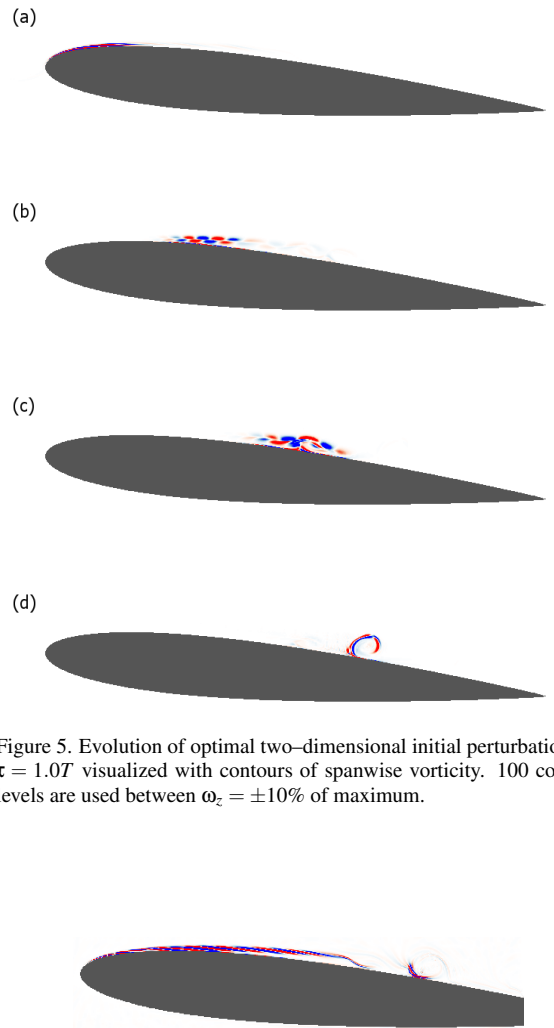


Figure 5. Evolution of optimal two-dimensional initial perturbation for $\tau = 1.0T$ visualized with contours of spanwise vorticity. 100 contour levels are used between $\omega_z = \pm 10\%$ of maximum.

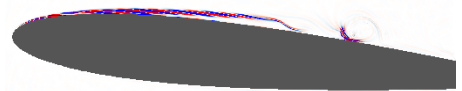


Figure 6. Optimal two-dimensional initial perturbation for $\tau = 0.25T$ visualized with contours of spanwise vorticity. 100 contour levels are used between $\omega_z = \pm 10\%$ of maximum.

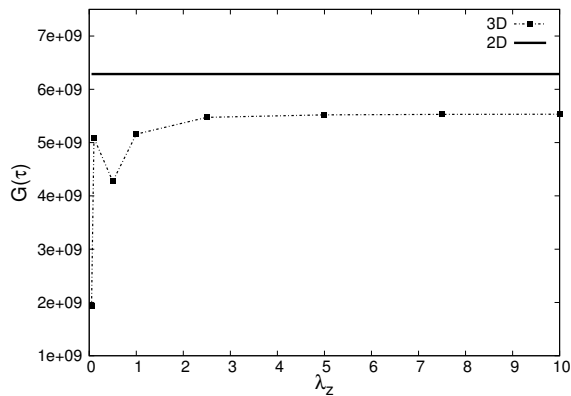


Figure 7. Optimal growth as a function of perturbation spanwise wavelength and comparison with optimal growth for two-dimensional perturbations. Time horizon is $\tau = 1.0T$.

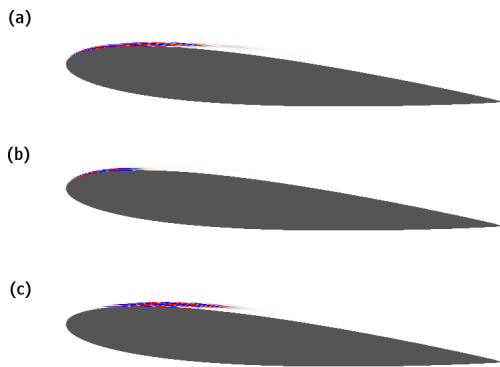


Figure 8. Optimal three-dimensional initial perturbations for (a) $\tau = 1.0T$, $\lambda_z = 0.1c$; (b) $\tau = 1.0T$, $\lambda_z = 10.0c$; and (c) $\tau = 0.25T$, $\lambda_z = 0.1c$. Contours are spanwise vorticity with 100 levels between $\omega_z = \pm 10\%$ of maximum.

turbations are seen to support larger transient growth with the optimal growth appearing to very slowly approach the growth for two-dimensional perturbations.

At wavelengths below $1.0c$, the optimal growth is observed to drop off sharply with a brief recovery at $\lambda_z = 0.1$. The sharp decay is perhaps due to sharper spanwise gradients in the low wavelength Fourier modes leading to enhanced viscous decay, while the recovery at $\lambda_z = 0.1$ may be due to the onset of a separate instability mechanism. In a study of transient growth in flat plate boundary layers, Monokroussos *et al.*[7] found that long spanwise wavelengths promoted the Orr mechanism while short wavelengths led to perturbation growth via lift-up.

Optimal initial conditions computed here suggest that, in this case, the dynamics are largely the same as the two-dimensional case. The initial conditions are still dominated by upstream tilted vortices as shown in figures 8a to 8c. Evolution of the initial conditions also shows similar flow development to the two-dimensional case. A possible explanation for the absence of lift-up is that the Reynolds number here is too low to support the fine scale structures found to support lift-up in [7].

Optimal initial conditions for short and long wavelength perturbations are shown in 8a and 8b respectively. For long wavelengths, the optimal initial condition is localized close to the leading edge while the short wavelength initial perturbation is longer and more closely localized to the separation point. This may suggest that the higher viscous decay rates associated with short wavelength perturbations reduces the effectiveness of per-

turbation growth through the Orr mechanism in the leading edge.

Comparing figures 8a and 8c suggests that the effect of reducing the optimization time is to push the optimal initial perturbation slightly downstream. This is similar to what was observed in the two-dimensional case except that no significant amplitude is observed in the base flow shed vorticity. This is possibly due to the perturbation growth mechanisms in the shed vorticity being more sensitive to the additional viscous damping associated with the shorter wavelengths.

Conclusions

In this work, the response of two-dimensional periodic flow over a NACA 0012 airfoil at $Re = 5 \times 10^4$ and $\alpha = 5^\circ$ to two and three-dimensional optimal initial perturbations is analysed. The flow was found to support strong transient growth in both cases with two-dimensional growth mechanisms appearing to be dominant. The Orr mechanism in the boundary layer upstream of the vortex shedding region of the base flow was observed to be a primary contributor to perturbation energy growth while base flow shed vorticity also appeared to be a site of significant energy amplification.

References

- [1] Abdessemed, N., Sherwin, S.J. & Theofilis V., Linear instability analysis of low-pressure turbine flows, *J. Fluid. Mech.*, **628**, 2009, 57–83.
- [2] Barkley, D., Blackburn, H.M. & Sherwin, S.J., Direct optimal growth analysis for timesteppers, *Int. J. Num. Methods Fluids*, **57**, 2008, 1435–1458.
- [3] Blackburn, H.M., & Sherwin, S.J. Formulation of a Galerkin spectral element-Fourier method for three-dimensional incompressible flows in cylindrical geometries, *J. Comp. Phys.*, **197**, 2004, 759–778.
- [4] Jones, L.E., Sandberg, R.D. & Sandham, N.D., Direct numerical simulations of forced and unforced separation bubbles on an airfoil at incidence, *J. Fluid. Mech.*, **602**, 2008, 175–207.
- [5] Jones, L.E., Sandberg, R.D. & Sandham, N.D., Stability and receptivity characteristics of a laminar separation bubble on an aerofoil, *J. Fluid. Mech.*, **648**, 2010, 257–296.
- [6] Kitsios, V., Rodriguez, D., Theofilis, V., Ooi, A. & Soria, J., BiGlobal stability analysis in curvilinear coordinates of massively separated lifting bodies, *J. Comp. Phys.*, **228**, 2009, 7181–7196.
- [7] Monokroussos, A., Akervik, E. Brandt, L. & Henningson, D.S., Global three-dimensional optimal disturbances in the Blasius boundary-layer flow using timesteppers, *J. Fluid. Mech.*, **650**, 2010, 181–214.
- [8] Sharma, A.S., Abdessemed, N., Sherwin, S.J. & Theofilis V., Transient growth mechanisms of low Reynolds number flow over a low-pressure turbine blade, *Theor. Comp. Fluid. Dyn.*, **25**, 2011, 19–30.
- [9] Theofilis V., Barkley, D. & Sherwin, S.J., Spectral/hp element technology for flow instability and control, *Aeronaut. J.*, **106**, 2002, 619–625.
- [10] Zaki, T.A., Wissink, J.G., Rodi, W. & Durbin, P.A., Direct numerical simulations of transition in a compressor cascade: the influence of free-stream turbulence, *J. Fluid. Mech.*, **665**, 2010, 57–98.